JCTC Journal of Chemical Theory and Computation

pubs.acs.org/JCTC Article

Benchmarking Quasiclassical Mapping Hamiltonian Methods for Simulating Electronically Nonadiabatic Molecular Dynamics

Xing Gao, Maximilian A. C. Saller, Yudan Liu, Aaron Kelly, Jeremy O. Richardson, and Eitan Geva*

Cite This: J. Chem. Theory Comput. 2020, 16, 2883−2895 Read Online

ACCESS | Metrics & More | Article Recommendations | Supporting Information

ABSTRACT: Quasi-classical mapping Hamiltonian methods have recently emerged as a promising approach for simulating electronically nonadiabatic molecular dynamics. The classical-like dynamics of the overall system within these methods makes them computationally feasible, and they can be derived based on well-defined semiclassical approximations. However, the existence of a variety of different quasi-classical mapping Hamiltonian methods necessitates a systematic comparison of their respective advantages and limitations. Such a benchmark comparison is presented in this paper. The approaches compared include the Ehrenfest method, the symmetrical quasi-classical (SQC) method, and five variations of the linearized semiclassical (LSC) method, three of which employ a modified identity operator. The comparison is based on a number of popular nonadiabatic model systems; the spin-boson model, a Frenkel biexciton model, and Tully's scattering models 1 and 2. The relative accuracy of the different methods is tested by comparing with quantum-mechanically exact results for the dynamics of the electronic populations and coherences. We find that LSC with the modified identity operator typically performs better than the Ehrenfest and standard LSC approaches. In comparison to SQC, these modified methods appear to be slightly more accurate for condensed phase problems, but for scattering models there is little distinction between them.

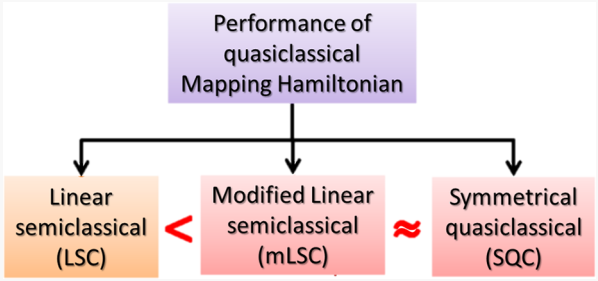

1. INTRODUCTION

Electronically nonadiabatic dynamical processes constitute an important class of inherently quantum-mechanical chemical phenomena that range from electronic energy and charge transfer to photochemistry.[1−12] Electronically nonadiabatic dynamics also underlies the functionality of many technologically- and biologically relevant systems ranging from photovoltaic devices[12−15] to the photosynthetic reaction center.[16−18]

The prohibitive computational cost of quantum-mechanically exact simulations of electronically nonadiabatic dynamics in complex molecular systems[19−22] has led to the development of a wide variety of approximate approaches,[23] including the Ehrenfest method,[24] surface hopping methods,[25−36] the mixed quantum-classical Liouville method,[37−44] the quantum-classical path integral method,[45−50] and quasi-classical mapping Hamiltonian (QC/MH) methods.[19,44,51−73] These approximate methods typically reduce the computational cost by describing the dynamics of the nuclear degrees of freedom (DOFs) and sometimes also of the electronic DOFs, in terms of classical-like trajectories.

In this paper we focus on QC/MH methods,[19,44,51−69] which represent the electronic population and coherence operators, whose expectation values correspond to the diagonal and off-diagonal electronic density matrix elements, respectively, using *mapping operators*. The latter have the same commutation relations as the original electronic operators. However, unlike the original operators, they are given in terms of auxiliary position and momentum operators and, as such, have a well-defined classical limit. Within the QC approximation, one typically treats the nuclear coordinates and momenta, as well as the above-mentioned auxiliary coordinates and momenta associated with the electronic DOFs, as classical-like. The dynamics of those phase-space variables is then dictated by classical-like Hamilton equations, with the Hamiltonian given by the classical limit of the mapped Hamiltonian in terms of the coordinates and momenta associated with the nuclear and electronic DOFs. The classical dynamics of the phase-space variables reproduces exactly the quantum dynamics of the bare electronic-state system, and the approximate nature of the result emanates from the classical treatment of the nuclear dynamics and their coupling to the electronic states.

It should be noted that QC/MH methods have been shown not to accurately capture nuclear quantum interference such as recurrences at longer times, due to the classical nature of the independent trajectory approximation.[74] For systems where such effects are relevant, more accurate methods such as

Received: December 19, 2019
Published: March 31, 2020

https://dx.doi.org/10.1021/acs.jctc.9b01267
J. Chem. Theory Comput. 2020, 16, 2883−2895

semiclassical initial value representation,[74,75] multiconfiguration time-dependent Hartree,[76] and matching pursuit or tensor-train split-operator Fourier transform[77,78] should be used. We would like to point out that mapping methods are most useful for the study of large systems, especially in the condensed phase, where the aforementioned more accurate methods are not feasible due to their exponential scaling with system size. We would also like to highlight that the systems studied in our work are models either for scattering or for large, condensed phase systems, which are known not to exhibit such effects.

Various QC/MH methods have been proposed, which differ with respect to the choice of mapping variables, as well as the sampling used to determine the values of the corresponding electronic variables at different times throughout the dynamics. The goal of this paper is to present a comprehensive comparison of different QC/MH methods. This comparison is based on a number of benchmark models (spin-boson, biexciton model,[60,79,80] and Tully's models[25]). The various mapping approaches compared include the Ehrenfest method, the symmetrical quasi-classical method (SQC), the linearized semiclassical method (LSC-IVR),[52,53] the Poisson-bracket mapping equation (PBME),[44,55,81] and three versions of the modified mapping approach recently proposed by Saller, Kelly, and Richardson.[62,63] The relative accuracy of these methods is tested by comparing their results with the quantum-mechanically exact dynamics of both the electronic populations and coherences.

The rest of this paper is organized as follows. The theoretical framework underlying QC/MH methods and the different formulations that lead to different methods are outlined in Section 2. The benchmark models used are described in Section 3. The results are presented and discussed in Section 4. Concluding remarks are given in Section 5.

2. THEORY

2.1. Preliminary Considerations. We focus on systems that can be described by a Hamiltonian of the following commonly encountered form:

$$\hat{H} = \frac{\hat{\mathbf{P}}^2}{2} + \sum_{\alpha',\alpha}^{N_e} V_{\alpha'\alpha}(\hat{\mathbf{R}})|\alpha'\rangle\langle\alpha| \tag{1}$$

Here, $\hat{\mathbf{P}} = (\hat{\mathbf{P}}_1, \hat{\mathbf{P}}_2 \cdots \hat{\mathbf{P}}_{N_n})$ and $\hat{\mathbf{R}} = (\hat{\mathbf{R}}_1, \hat{\mathbf{R}}_2 \cdots \hat{\mathbf{R}}_{N_n})$ denote the N_n mass-weighted coordinates and momenta of the nuclear DOFs. The electronic Hilbert space is spanned by $\{|\alpha\rangle\}$ for $\alpha = 1, \ldots, N_e$, which is assumed to constitute an orthonormal $\mathbf{R}$-independent basis, also known as a diabatic basis. It should however be noted that none of the QC/MH methods under consideration are limited to this type of basis.[82] Here we choose to work in terms of such a basis since the benchmark models we use are given in this form.

Within this representation, $\{|\alpha\rangle\langle\alpha|\}$ corresponds to electronic population operators, and $\{|\alpha\rangle\langle\alpha'|\}$ corresponds to electronic coherence operators ($\alpha \neq \alpha'$). $V_{\alpha\alpha}(\hat{\mathbf{R}})$ is the potential energy surface (PES) associated with the α-th electronic state, and $V_{\alpha\alpha'}(\hat{\mathbf{R}})$ is the electronic coupling between the α-th and the α'-th electronic states ($\alpha \neq \alpha'$). Some of our models also make use of the Condon approximation, which corresponds to replacing the electronic coupling operator $V_{\alpha\alpha'}(\hat{\mathbf{R}})$ by the constant electronic coupling coefficient $V_{\alpha\alpha'}$. This however is not a restriction for the approaches we discuss here.

We will study initial states of the overall system that have the following form:

$$\hat{\rho}(0) = \hat{\rho}_n(0) \otimes \hat{\sigma}(0) \tag{2}$$

Here, $\hat{\rho}_n(0) = \mathrm{Tr}_e[\hat{\rho}(0)]$ and $\hat{\sigma}(0) = \mathrm{Tr}_n[\hat{\rho}(0)]$ are the reduced density operators that describe the initial states of the nuclear DOFs and electronic DOFs, respectively ($\mathrm{Tr}_e[\cdot]$ and $\mathrm{Tr}_n[\cdot]$ stand for partially tracing over the electronic Hilbert space and the nuclear Hilbert space, respectively). Note that we choose both $\hat{\rho}_n(0)$ and $\hat{\sigma}(0)$ to be normalized such that $\mathrm{Tr}_n[\hat{\rho}_n(0)] = 1$ and $\mathrm{Tr}_e[\hat{\sigma}(0)] = 1$. For the sake of concreteness, we will also restrict ourselves to the commonly encountered case where $\hat{\sigma}(0) = |\lambda\rangle\langle\lambda|$, which implies that the initial state of the electronic DOFs corresponds to being in one of the basis states, $\{|\alpha\rangle\}$.

The state of the electronic DOFs at a later time t is then given by the electronic reduced density operator

$$\hat{\sigma}(t) = \mathrm{Tr}_n[\hat{\rho}(t)] = \sum_{\alpha\alpha'} \sigma_{\alpha\alpha'}(t)|\alpha\rangle\langle\alpha'| \tag{3}$$

where

$$\begin{aligned}\sigma_{\alpha\alpha'}(t) &= \mathrm{Tr}[\hat{\rho}_n(0)|\lambda\rangle\langle\lambda|e^{i\hat{H}t/\hbar}|\alpha'\rangle\langle\alpha|e^{-i\hat{H}t/\hbar}] \\ &\equiv C_{\hat{M}_{\lambda\lambda}\hat{M}_{\alpha'\alpha}}(t)\end{aligned} \tag{4}$$

is the $\alpha\alpha'$ electronic density matrix element. Here, $\mathrm{Tr}[\cdots] \equiv \mathrm{Tr}_n[\mathrm{Tr}_e[\cdots]]$ is the overall (electronic + nuclear) trace, $\hat{M}_{\alpha'\alpha} \equiv |\alpha'\rangle\langle\alpha|$, and $C_{\hat{A}\hat{B}}(t)$ is the correlation function defined by

$$C_{\hat{A}\hat{B}}(t) = \mathrm{Tr}\left[\hat{\rho}_n(0)\hat{A}e^{i\hat{H}t/\hbar}\hat{B}e^{-i\hat{H}t/\hbar}\right] \tag{5}$$

Importantly, $\sigma_{\alpha\alpha}(t)$ corresponds to the population of the α-th electronic state, and $\sigma_{\alpha'\alpha}(t)$ corresponds to the electronic coherence between the α'-th and α-th electronic states ($\alpha \neq \alpha'$).

Following refs 62 and 63, we also note that the electronic population operator can be cast in the following alternative form, as the sum of the identity operator, $\hat{1}$, and a traceless term

$$|\alpha\rangle\langle\alpha| = \frac{1}{N_e}(\hat{1} + \hat{Q}_\alpha) \tag{6}$$

where

$$\hat{Q}_\alpha = N_e\hat{M}_{\alpha\alpha} - \sum_{\alpha'}^{N_e} \hat{M}_{\alpha'\alpha'} \tag{7}$$

As a result, one can cast the electronic populations and coherences in the following alternative, yet completely equivalent, form:

$$\sigma_{\alpha\alpha}(t) = \frac{1}{N_e^2}[N_e + C_{\hat{1}\hat{Q}_\alpha}(t) + C_{\hat{Q}_\alpha\hat{Q}_\alpha}(t)] \tag{8}$$

$$\sigma_{\alpha\alpha'}(t) = \frac{1}{N_e}[C_{\hat{1}\hat{M}_{\alpha'\alpha}}(t) + C_{\hat{Q}_\alpha\hat{M}_{\alpha'\alpha}}(t)] \tag{9}$$

2.2. Mapping Variables and the Quasiclassical Approximation. MH methods are often based on casting the electronic population and coherence operators, $\{|\alpha'\rangle\langle\alpha|\}$, onto an isomorphic set of operators, $\{M_{\alpha'\alpha}(\hat{\mathbf{q}}, \hat{\mathbf{p}})\}$, that satisfy the same commutation relations:[19,52,53,55,62−68,68,69,80−91]

https://dx.doi.org/10.1021/acs.jctc.9b01267
J. Chem. Theory Comput. 2020, 16, 2883−2895

$$|\alpha'\rangle\langle\alpha| \rightarrow M_{\alpha'\alpha}(\hat{\mathbf{q}}, \hat{\mathbf{p}}) \tag{10}$$

Here, $\{\hat{\mathbf{q}}, \hat{\mathbf{p}}\}$ represents a set of auxiliary Cartesian coordinate and momentum operators associated with the mapping (not to be confused with the coordinate and momentum operators of the actual electrons). The motivation for replacing the original set of electronic operators with the mapping operators can be traced back to the fact that unlike $\{|\alpha'\rangle\langle\alpha|\}$, $\{M_{\alpha'\alpha}(\hat{\mathbf{q}}, \hat{\mathbf{p}})\}$ has classical-like analogues. As a result, QC approximations become possible.

The actual choice of mapping variables is not unique, and multiple choices of mapping variables have been proposed and employed.[68−70,80,82,87,92−94] In this paper, we focus on methods based on the mapping proposed by Stock and Thoss[51] (sometimes also referred to in the literature as the Meyer-Miller mapping, due to its similarity to the mapping proposed earlier by Meyer and Miller[19]).

Within this Meyer-Miller-Stock-Thoss (MMST) mapping, one represents the system of N_e electronic states, $\{|\alpha\rangle\}$, in terms of an isomorphic system of N_e independent harmonic modes with creation and annihilation operators $\{\hat{c}_\alpha^\dagger\}$ and $\{\hat{c}_\alpha\}$, respectively, such that $[\hat{c}_\alpha, \hat{c}_{\alpha'}^\dagger] = \delta_{\alpha\alpha'}$. The electronic operators, $\{|\alpha'\rangle\langle\alpha|\}$ (with $\alpha = \alpha'$ for populations and $\alpha \neq \alpha'$ for coherences), can then be mapped onto the harmonic oscillator operators $\{\hat{c}_{\alpha'}^\dagger \hat{c}_\alpha\}$, which satisfy the same commutation relations. $\hat{c}_\alpha^\dagger$ and $\hat{c}_\alpha$ can also be cast in terms of Cartesian coordinates, $\{\hat{q}_\alpha\}$, and momenta, $\{\hat{p}_\alpha\}$, such that $\hat{c}_\alpha^\dagger = \frac{1}{\sqrt{2\hbar}}(\hat{q}_\alpha - i\hat{p}_\alpha)$ and $\hat{c}_\alpha = \frac{1}{\sqrt{2\hbar}}(\hat{q}_\alpha + i\hat{p}_\alpha)$. This results in the following expressions for the electronic population and coherence operators in terms of $\{\hat{q}_\alpha, \hat{p}_\alpha\}$:

$$\begin{aligned}
\hat{M}_{\alpha\alpha} &\rightarrow \frac{1}{2\hbar}(\hat{q}_\alpha^2 + \hat{p}_\alpha^2 - \hbar) \\
\hat{M}_{\alpha'\alpha} &\rightarrow \frac{1}{2\hbar}(\hat{q}_\alpha\hat{q}_{\alpha'} + \hat{p}_\alpha\hat{p}_{\alpha'} - i\hat{q}_\alpha\hat{p}_{\alpha'} + i\hat{p}_\alpha\hat{q}_{\alpha'})
\end{aligned} \tag{11}$$

We denote the mapping relations in eq 11 as *mapping #1*.

An alternative mapping can be obtained by noting that the quantum dynamics in terms of the MMST mapping variables is restricted to the subspace spanned by the singly excited states, $\{|0_1, 0_2, ..., 1_\alpha, ..., 0_{N_e}\rangle\}$. Here, $|0_1, 0_2, ..., 1_\alpha, ..., 0_{N_e}\rangle$ corresponds to the α-th mode being in the first excited state, while all the other modes are in the ground state. This leads to the following mapping of the electronic population and coherence operators:

$$\hat{M}_{\alpha'\alpha} \rightarrow \left|0_1, 0_2, ..., 1_{\alpha'}, ..., 0_{N_e}\right\rangle\left\langle 0_{N_e}, ..., 1_\alpha, ..., 0_2, 0_1\right| \tag{12}$$

We denote the mapping relations in eq 12 as *mapping #2*.

Applying the linearized semiclassical (LSC) approximation[41,95−105] to eq 5 leads to the following QC approximation for the correlation function $C_{\hat{A}\hat{B}}(t)$:

$$\begin{aligned}
C_{\hat{A}\hat{B}}(t) \approx \left(\frac{1}{2\pi\hbar}\right)^N \int d\mathbf{R}_0 \int d\mathbf{P}_0 \int d\mathbf{q}_0 \int d\mathbf{p}_0 \\
\times [\hat{\rho}_n(0)]_W(\mathbf{R}_0, \mathbf{P}_0) A_W(\mathbf{q}_0, \mathbf{p}_0) B_W(\mathbf{q}_t, \mathbf{p}_t)
\end{aligned} \tag{13}$$

Here, $N = N_e + N_n$ is the total number of DOFs of the overall system, while $[\hat{\rho}_n(0)]_W(\mathbf{R}, \mathbf{P})$ and $A_W(\mathbf{q}_0, \mathbf{p}_0)$ are the Wigner transform of the nuclear operator $\hat{\rho}_n(0)$ and electronic operator $\hat{A}$, respectively:

$$\begin{aligned}
A_W(\mathbf{q}, \mathbf{p}) &= \int d\mathbf{z} e^{-i\mathbf{z}\mathbf{p}/\hbar}\left\langle \mathbf{q} + \frac{\mathbf{z}}{2}\middle| A(\hat{\mathbf{q}}, \hat{\mathbf{p}})\middle| \mathbf{q} - \frac{\mathbf{z}}{2}\right\rangle \\
[\hat{\rho}_n(0)]_W(\mathbf{R}, \mathbf{P}) &= \int d\mathbf{Z} e^{-i\mathbf{Z}\mathbf{P}/\hbar}\left\langle \mathbf{R} + \frac{\mathbf{Z}}{2}\middle| \hat{\rho}_n(0)\middle| \mathbf{R} - \frac{\mathbf{Z}}{2}\right\rangle
\end{aligned} \tag{14}$$

Importantly, $\{\mathbf{R}_t, \mathbf{P}_t, \mathbf{q}_t, \mathbf{p}_t\}$ is obtained by starting at the initial state $\{\mathbf{R}_0, \mathbf{P}_0, \mathbf{q}_0, \mathbf{p}_0\}$ and evolving a *classical* trajectory by solving Hamilton's equations based on the classical limit of the overall system Hamiltonian in eq 1. In what follows we use the symmetrized mapping Hamiltonian, which has also been used in previous studies[19,55,62,63]

$$\begin{aligned}
&H(\mathbf{R}, \mathbf{P}, \mathbf{q}, \mathbf{p}) \\
&= \frac{\mathbf{P}^2}{2} + \bar{V}(\mathbf{R}) + \frac{1}{2\hbar}\sum_\alpha^{N_e}(V_{\alpha\alpha}(\mathbf{R}) - \bar{V}(\mathbf{R}))(q_\alpha^2 + p_\alpha^2) \\
&\quad + \frac{1}{2\hbar}\sum_{\alpha\neq\alpha'}^{N_e} V_{\alpha\alpha'}(\mathbf{R})(q_\alpha - ip_\alpha)(q_{\alpha'} + ip_{\alpha'})
\end{aligned} \tag{15}$$

where $\bar{V} = \frac{1}{N_e}\sum_\alpha V_{\alpha\alpha}(\mathbf{R})$. In this way, the resulting diabatic potential matrix is traceless. It also removes the zero-point energy terms (resulting from the commutation relations of $\hat{q}_\alpha$ and $\hat{p}_\alpha$) from the Hamiltonian.

Applying the LSC approximation within mapping #1 (see eq 11) yields the following QC phase-space variables for the electronic populations and coherences:

$$\begin{aligned}
[\hat{M}_{\alpha\alpha}]_W^{(\mathrm{I})}(\mathbf{q}, \mathbf{p}) &= \frac{1}{2\hbar}[q_\alpha^2 + p_\alpha^2 - \hbar] \\
[\hat{M}_{\alpha'\alpha}]_W^{(\mathrm{I})}(\mathbf{q}, \mathbf{p}) &= \frac{1}{2\hbar}[q_\alpha + ip_\alpha][q_{\alpha'} - ip_{\alpha'}]
\end{aligned} \tag{16}$$

Applying the LSC approximation within mapping #2 (see eq 12) yields the following QC phase-space variables for the electronic populations and coherences

$$\begin{aligned}
[\hat{M}_{\alpha\alpha}]_W^{(\mathrm{II})}(\mathbf{q}, \mathbf{p}) &= \phi(\mathbf{q}, \mathbf{p})\left[q_\alpha^2 + p_\alpha^2 - \frac{\hbar}{2}\right] \\
[\hat{M}_{\alpha'\alpha}]_W^{(\mathrm{II})}(\mathbf{q}, \mathbf{p}) &= \phi(\mathbf{q}, \mathbf{p})[q_\alpha + ip_\alpha][q_{\alpha'} - ip_{\alpha'}]
\end{aligned} \tag{17}$$

where

$$\phi(\mathbf{q}, \mathbf{p}) = \frac{2^{N_e+1}}{\hbar}\exp -\frac{1}{\hbar}\sum_{\alpha'=1}^{N_e}(q_{\alpha'}^2 + p_{\alpha'}^2) \tag{18}$$

At least five different implementations of the above-mentioned mapping LSC scheme have been proposed. The first two implementations are based on applying the LSC approximation in eq 13 to the correlation function $C_{\hat{M}_{\lambda\lambda}\hat{M}_{\alpha'\alpha}}(t)$ in eq 4. Both implementations use mapping #2 for $\hat{M}_{\lambda\lambda}$ (the mapping variable evaluated at the initial time). This is because, even within a fully quantum description, one needs to project onto the physical subspace at least once. Additionally, $\phi(\mathbf{q}, \mathbf{p})$, eq 18, provides a well-defined phase-space density for initial sampling of $(\mathbf{q}_0, \mathbf{p}_0)$. The two implementations differ with respect to which mapping they use for $\hat{M}_{\alpha'\alpha}$ (the mapping

https://dx.doi.org/10.1021/acs.jctc.9b01267
J. Chem. Theory Comput. 2020, 16, 2883−2895

variable evaluated at time t). Using mapping #1 for $\hat{M}_{\alpha'\alpha}$ leads to an implementation we denote as LSCI (sometimes also referred to as PBME[81]). Using mapping #2 for $\hat{M}_{\alpha'\alpha}$ leads to an implementation we denote as LSCII (sometimes also referred to as LSC-IVR[52,53]). A summary of how to calculate correlation functions of the form $C_{\hat{A}\hat{B}}(t)$ for these mapping approaches can be found in Table SI of the Supporting Information.

The third and fourth implementations, introduced in ref 62, are based on applying the LSC approximation in eq 13 to the correlation functions $C_{\hat{1}\hat{Q}_\alpha}(t), C_{\hat{1}\hat{M}_{\alpha'\alpha}}(t), C_{\hat{Q}_\lambda\hat{Q}_\alpha}(t)$, and $C_{\hat{Q}_\lambda\hat{M}_{\alpha'\alpha}}(t)$ in eqs 8 and 9. These modified LSC implementations approximate $C_{\hat{1}\hat{Q}_\alpha}(t)$ and $C_{\hat{1}\hat{M}_{\alpha'\alpha}}(t)$ by mapping $\hat{1}$ onto 1 and using mapping #2 for $\hat{Q}_\alpha$ and $\hat{M}_{\alpha'\alpha}$. However, they differ with respect to how they approximate $C_{\hat{Q}_\lambda\hat{Q}_\alpha}(t)$ and $C_{\hat{Q}_\lambda\hat{M}_{\alpha'\alpha}}(t)$. Using mapping #2 for $\hat{Q}_\lambda$ and mapping #1 for $\hat{Q}_\alpha$ and $\hat{M}_{\alpha'\alpha}$ leads to an implementation that we denote as mLSC/$\phi^1\phi^1$. Using mapping #2 for $\hat{Q}_\lambda$, $\hat{Q}_\alpha$, and $\hat{M}_{\alpha'\alpha}$ leads to an implementation that we denote as mLSC/$\phi^1\phi^2$.

A fifth possible implementation proposed in ref 62 corresponds to applying the LSC approximation in eq 13 to the correlation functions $C_{\hat{1}\hat{Q}_\alpha}(t)$, $C_{\hat{1}\hat{M}_{\alpha'\alpha}}(t)$, $C_{\hat{Q}_\lambda\hat{Q}_\alpha}(t)$, and $C_{\hat{Q}_\lambda\hat{M}_{\alpha'\alpha}}(t)$ in eq 8, using mapping #2 for $\hat{Q}_\lambda$, $\hat{Q}_\alpha$, and $\hat{M}_{\alpha'\alpha}$ and also mapping $\hat{1}$ onto $2\hbar\phi(\mathbf{q}, \mathbf{p})$. We denote this implementation as mLSC/$\phi^2\phi^2$.

It is worth noting that, both the $\hat{Q}_k$ and $\hat{M}_{\alpha'\alpha}$ operators (for $\alpha \neq \alpha'$) are traceless and therefore do not contain zero-point energy terms arising from the commutators of the harmonic-oscillator mapping variables. As a result of this, the difference between mapping #1 and #2 for both operators is simply a factor of $2\hbar\phi(\mathbf{q}, \mathbf{p})$. The advantage of the mLSC methods lies in the splitting of the electronic population operators into the identity and the traceless $\hat{Q}_k$ operator. By mapping the identity operator to 1, the potential errors associated with the zero-point energy terms in the traditional LSC methods is thereby avoided. A summary of how to calculate correlation functions of the form $C_{\hat{A}\hat{B}}(t)$ for these mapping approaches can be found in Table SII of the Supporting Information.

The SQC method proposed by Miller and co-workers can also be viewed as alternative implementation of the LSC approximation.[56−61] This method is usually formulated in terms of action-angle (a-a) variables, rather than in terms of the above-mentioned Cartesian coordinates and momenta.[19,80] Each electronic state $|\alpha\rangle$ is associated with a classical harmonic mode whose state is given by the corresponding action, n_α, and angle, u_α, variables. Semiclassical expressions for the ground and first excited wave functions of the α-th harmonic mode in terms of a-a variables are given by $\psi_0(u_\alpha) = \frac{1}{\sqrt{2\pi}}$ and $\psi_1(u_\alpha) = \frac{1}{\sqrt{2\pi}}e^{iu_\alpha}$, respectively.[80] Furthermore, the Wigner transform can also be cast in terms of a-a variables:

$$A_W(\mathbf{n}, \mathbf{u}) = \int \mathbf{dy} e^{-i\mathbf{yn}} \left\langle \mathbf{u} + \frac{\mathbf{y}}{2} \middle| \hat{A} \middle| \mathbf{u} - \frac{\mathbf{y}}{2} \right\rangle \tag{19}$$

Here $\mathbf{n} = (n_1, ..., n_{N_e})$ and $\mathbf{u} = (u_1, ..., u_{N_e})$. Substituting $\hat{M}_{\alpha'\alpha}$ from eq 12 for $\hat{A}$ in eq 19 then yields the following QC a-a variables for the electronic populations and coherences:

$$[\hat{M}_{\alpha\alpha}]_W^{(\mathrm{SQC})}(\mathbf{n}, \mathbf{u}) = \delta(n_\alpha - 1) \prod_{\alpha' \neq \alpha}^{N_e} \delta(n_{\alpha'})$$

$$[\hat{M}_{\alpha'\alpha}]_W^{(\mathrm{SQC})}(\mathbf{n}, \mathbf{u}) = e^{i(u_\alpha - u_{\alpha'})}\delta\left(n_\alpha - \frac{1}{2}\right) \times \delta\left(n_{\alpha'} - \frac{1}{2}\right) \prod_{\beta \neq \alpha,\alpha'}^{N_e} \delta(n_\beta) \tag{20}$$

The SQC method is based on replacing the delta functions in action space (see eq 20) with prelimit delta functions. One such choice, which gives rise to square window functions in action space, is based on replacing $\delta(n_\alpha - a)$ with $h(\gamma - |n_\alpha - a|)/2\gamma$, for a given γ, where

$$h(x) = \begin{cases} 1 & x \geq 0 \\ 0 & x < 0 \end{cases} \tag{21}$$

Another choice leads to triangular window functions.[61] The a-a variables are related to the corresponding Cartesian coordinates and momenta in the following manner:

$$q_\alpha = \sqrt{2\hbar(n_\alpha + \gamma)}\, \cos(u_\alpha)$$

$$p_\alpha = \sqrt{2\hbar(n_\alpha + \gamma)}\, \sin(u_\alpha) \tag{22}$$

Miller and co-workers have recommended setting the value of the width parameter, γ, to 0.366, since this value has been observed to give the most accurate results when the method is applied to benchmark models and can be justified from a consideration of mapping to a spin-1/2 system.[56,70] It was also reported that replacing the above-mentioned square window function with a triangular window function can lead to more accurate results as well as better convergence.[61] The SQC calculations reported in this paper were based on using such triangular window functions.

The Ehrenfest (mean-field) method can also be cast as a QC/MH-type method.[19] In this case, the electronic state at time t is given by

$$|\psi(t)\rangle = \sum_\alpha^{N_e} c_\alpha(t)|\alpha\rangle \tag{23}$$

and the dynamics of the coefficients, $\{c_\alpha(t)\}$, are dictated by

$$\dot{c}_\alpha(t) = -\frac{i}{\hbar}\sum_{\alpha'}^{N_e} V_{\alpha\alpha'}(\mathbf{R}_t)c_{\alpha'}(t) \tag{24}$$

Here, $\mathbf{R}_t$ is the nuclear coordinates at time t, which are treated classically. The mean-field approximation is introduced by assuming that the dynamics $\mathbf{R}_t$ is governed by the mean-field PES, $\langle\psi(t)|\hat{V}|\psi(t)\rangle$. Letting

$$c_\alpha = \frac{1}{\sqrt{2\hbar}}(q_\alpha + ip_\alpha) \tag{25}$$

it can be shown that Ehrenfest dynamics is equivalent to propagating $\{\mathbf{R}_t, \mathbf{P}_t, \mathbf{q}_t, \mathbf{p}_t\}$ as classical variables subject to the classical Hamiltonian in eq 15.[19] However, in this case $\{\mathbf{q}_0, \mathbf{p}_0\}$ is uniquely determined by $c_\alpha(0)$, as opposed to LSC and SQC where there is an initial distribution of initial $\{\mathbf{q}_0, \mathbf{p}_0\}$.

The mapping Hamiltonian methods outlined above are summarized in Figure 1.

3. MODELS

Below, we compare results obtained by applying the above-mentioned seven methods (LSCI, LSCII, mLSC/$\phi^1\phi^1$, mLSC/

https://dx.doi.org/10.1021/acs.jctc.9b01267
J. Chem. Theory Comput. 2020, 16, 2883−2895

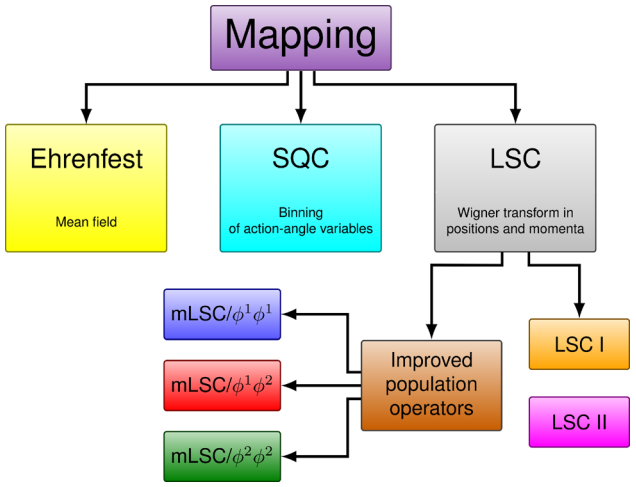

Figure 1. Mapping Hamiltonian methods studied in this work.

$\phi^1\phi^2$, mLSC/$\phi^2\phi^2$, SQC, and Ehrenfest) to the following benchmark models, for which quantum-mechanically exact results can be obtained: (1) the spin-boson model; (2) a Frenkel biexciton model; and (3) Tully's models 1 and 2.

All models are based on a Hamiltonian of the form of eq 1 and include two electronic states ($N_e = 2$), which we will denote $|1\rangle$ and $|2\rangle$. We assume that the system starts out in state $|1\rangle$, so that $\hat{\sigma}(0) = |1\rangle\langle 1|$. For each model, we compare the expectation values of $\langle\hat{\sigma}_x(t)\rangle$, $\langle\hat{\sigma}_y(t)\rangle$, and $\langle\hat{\sigma}_z(t)\rangle$ as obtained via the above-mentioned methods. Here, $\hat{\sigma}_x = |1\rangle\langle 2| + |2\rangle\langle 1|$, $\hat{\sigma}_y = -i|1\rangle\langle 2| + i|2\rangle\langle 1|$, and $\hat{\sigma}_z = |1\rangle\langle 1| - |2\rangle\langle 2|$. These expectation values are defined by $\langle\hat{\sigma}_i(t)\rangle = \mathrm{Tr}[\rho_n(0)|1\rangle\langle 1|\hat{\sigma}_i(t)]$. $\langle\hat{\sigma}_z(t)\rangle$ corresponds to the population difference, while $\langle\hat{\sigma}_x(t)\rangle$ and $\langle\hat{\sigma}_y(t)\rangle$ correspond to the real and imaginary parts of the coherence. Note that we set $\hbar = 1$ throughout the following sections.

3.1. Spin-Boson Model. For the spin-boson model

$$V_{11}(\mathbf{R}) = \sum_{k=1}^{N_n}\frac{1}{2}\omega_k^2 R_k^2 + \sum_{k=1}^{N_n} g_k R_k + \epsilon$$
$$V_{22}(\mathbf{R}) = \sum_{k=1}^{N_n}\frac{1}{2}\omega_k^2 R_k^2 - \sum_{k=1}^{N_n} g_k R_k - \epsilon$$
$$V_{12}(\mathbf{R}) = V_{21}(\mathbf{R}) = \Delta \tag{26}$$

The frequencies of the harmonic nuclear modes and corresponding coupling coefficients, $\{\omega_k\}$ and $\{g_k\}$, respectively, are obtained from the Ohmic spectral density

$$J(\omega) = \frac{\pi}{2}\sum_k^{N_n}\frac{g_k^2}{\omega_k}\delta(\omega - \omega_k) \to \frac{\pi}{2}\eta\omega e^{-\omega/\omega_c} \tag{27}$$

following the discretization approach outlined in ref 106. Here the Kondo parameter η and cutoff frequency ω_c are related to the reorganization energy $\zeta = 2\eta\omega_c$ which characterizes the overall electron−phonon coupling strength. The initial state of the nuclear DOFs is given by $\hat{\rho}_n(0) = e^{-\beta\hat{H}_0}/\mathrm{Tr}_n(e^{-\beta\hat{H}_0})$ with $\hat{H}_0 = \sum_{k=1}^{N_n}\frac{1}{2}[\hat{P}_k^2 + \omega_k^2\hat{R}_k^2]$.

Below, we report results obtained for the following four sets of parameters: (a) symmetric high T: $\epsilon = 0$, $\Delta = 1$, $\eta = 0.09$, $\omega_c = 2.5$, $\beta = 0.1$; (b) symmetric low T: $\epsilon = 0$, $\Delta = 1$, $\eta = 0.09$, $\omega_c = 2.5$, $\beta = 5$; (c) asymmetric high T: $\epsilon = 1$, $\Delta = 1$, $\eta = 0.1$, $\omega_c = 1$, $\beta = 0.25$; (d) asymmetric low T: $\epsilon = 1$, $\Delta = 1$, $\eta = 0.1$, $\omega_c = 2$, $\beta = 5$. We have also included a parameter set corresponding to the critical damping regime in the Supporting Information: $\epsilon = 1$, $\Delta = 1$, $\eta = 0.4$, $\omega_c = 2$, $\beta = 5$. This particular parameter set has previously been studied using mapping approaches, see for example refs 107 and 62. Compared to the parameters in (d), the Kondo parameter is increased from 0.1 to 0.4 with overall coupling strength ζ/Δ increased from 0.4 to 1.6.

3.2. Frenkel Biexciton Model. For the Frenkel biexciton model

$$V_{11}(\mathbf{R}) = \epsilon_1 + \sum_k^{N_n}\frac{1}{2}\omega_k^2(R_{k,1} - D_k)^2 + \sum_k^{N_n}\frac{1}{2}\omega_k^2 R_{k,2}^2$$
$$V_{22}(\mathbf{R}) = \epsilon_2 + \sum_k^{N_n}\frac{1}{2}\omega_k^2(R_{k,2} - D_k)^2 + \sum_k^{N_n}\frac{1}{2}\omega_k^2 R_{k,1}^2$$
$$V_{12}(\mathbf{R}) = V_{21}(\mathbf{R}) = \Delta \tag{28}$$

Here, ϵ_k denotes the k-th site energy ($k = 1, 2$). Each site is coupled to an independent bath with N_n harmonic modes. The displacements $\{D_k\}$ are given by $D_k = g_k/\omega_k^2$. $\{\omega_k\}$ and $\{g_k\}$ are obtained from the Debye spectral density

$$J(\omega) = \frac{\pi}{2}\sum_k^{N_n}\frac{g_k^2}{\omega_k}\delta(\omega - \omega_k) \to 2\zeta\frac{\omega\omega_c}{\omega^2 + \omega_c^2} \tag{29}$$

following the discretization approach outlined in ref 106. Here ζ denotes reorganization energy. Again, the initial state of the nuclear DOFs is given by $\hat{\rho}_n(0) = e^{-\beta\hat{H}_0}/\mathrm{Tr}_n(e^{-\beta\hat{H}_0})$ with $\hat{H}_0 = \sum_{k=1}^{N_n}\frac{1}{2}[\hat{P}_k^2 + \omega_k^2\hat{R}_k^2]$.

Below, we report calculations for this model with the following parameters: $\epsilon_1 = 50\ \mathrm{cm}^{-1}$, $\epsilon_2 = -50\ \mathrm{cm}^{-1}$, $\Delta = 100\ \mathrm{cm}^{-1}$, $\omega_c = 200\ \mathrm{cm}^{-1}$, $T = 72$ K, and $\zeta = 10$, 50, or $150\ \mathrm{cm}^{-1}$, where the strength of coupling to the environment can be measured respectively through the coefficients $\zeta/\Delta = 0.1$, 0.5, and 1.5.

3.3. Tully's Models 1 and 2. For Tully's single avoided crossing model 1[25]

$$V_{11}(R) = \begin{cases} A[1 - \exp(-BR)] & R > 0 \\ -A[1 - \exp(BR)] & R < 0 \end{cases}$$
$$V_{22}(R) = -V_{11}(R)$$
$$V_{12}(R) = V_{21}(R) = C\exp(-DR^2) \tag{30}$$

with $A = 0.01$, $B = 1.6$, $C = 0.005$, and $D = 1.0$.

For Tully's dual avoided crossing model 2[25]

$$V_{11}(R) = 0$$
$$V_{12}(R) = -A\exp(-BR^2) + E_0$$
$$V_{12}(R) = V_{21}(R) = C\exp(-DR^2) \tag{31}$$

with $A = 0.10$, $B = 0.28$, $C = 0.015$, $D = 0.06$, and $E_0 = 0.05$.

For these models, we calculate the final population of the two channels as a function of the initial momentum.[25] The initial nuclear coordinate is sampled according to the

https://dx.doi.org/10.1021/acs.jctc.9b01267
J. Chem. Theory Comput. 2020, 16, 2883−2895

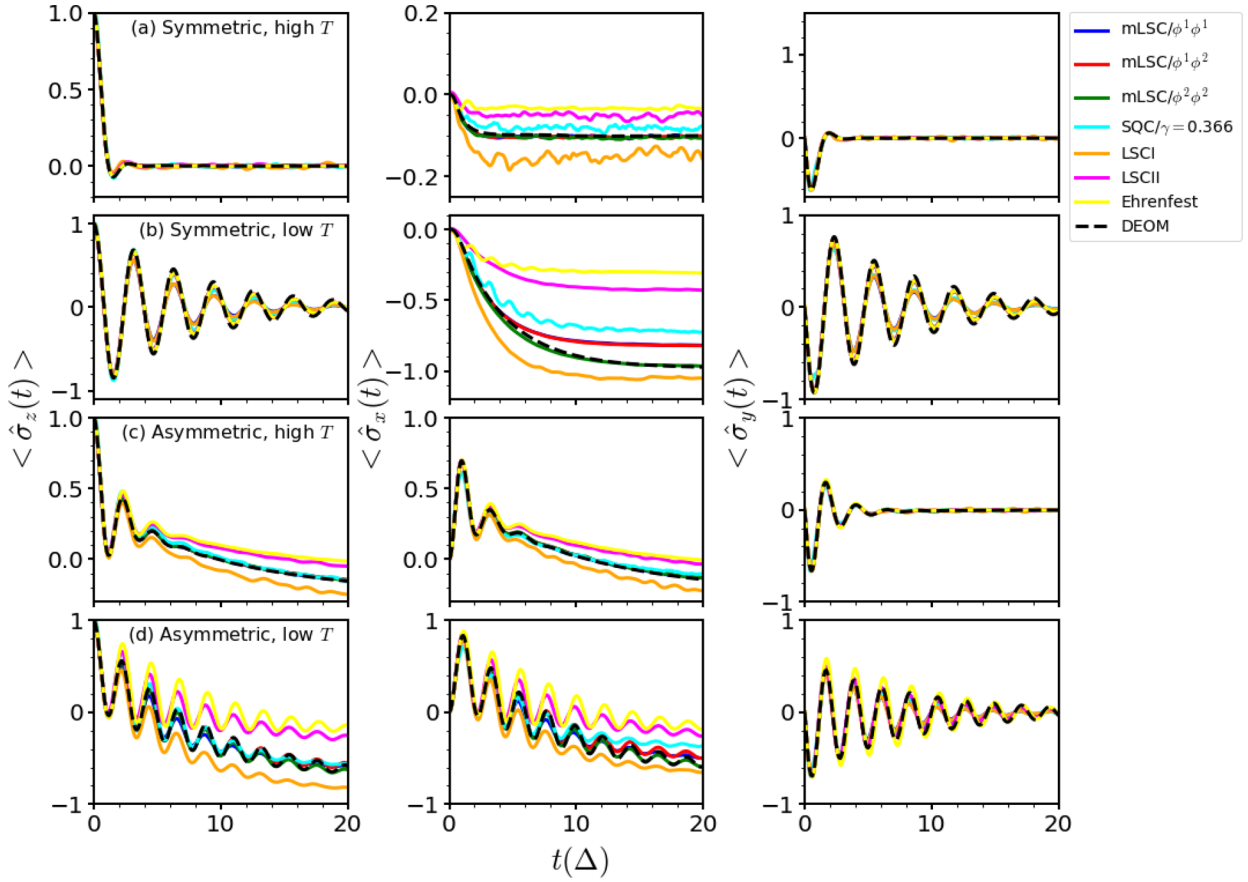

Figure 2. Population and coherence dynamics of spin-boson models with variant parameters: (a) $\epsilon = 0$, $\Delta = 1$, $\eta = 0.09$, $\omega_c = 2.5$, $\beta = 0.1$; (b) $\epsilon = 0$, $\Delta = 1$, $\eta = 0.09$, $\omega_c = 2.5$, $\beta = 5$; (c) $\epsilon = 1$, $\Delta = 1$, $\eta = 0.1$, $\omega_c = 1$, $\beta = 0.25$; and (d) $\epsilon = 1$, $\Delta = 1$, $\eta = 0.1$, $\omega_c = 2$, $\beta = 5$. In SQC, we employ triangular windows with width $\gamma = 0.366$.

Wigner transform of a Gaussian wavepacket[29] $\exp(iP_0R)\exp[-(R - R_0)^2/\sigma^2]$, with $R_0 = -20$, P_0 is the initial momentum, and $\sigma = 20/P_0$. The nuclear mass is set to 2000 au.[25] The simulation of the mapping variables was performed in the diabatic representation starting in the lower diabatic state. The asymptotic populations in the transmission channels of ground adiabatic state (T1) and excited state (T2) are then calculated.

In addition, we also calculate the population and coherence dynamics. To this end, we start out with $R_0 = -9, \sigma = \sqrt{2}$ for a range of values of P_0, and in each case sample R_0 is based on $\exp\left(-\frac{\sigma^2}{2}(P - P_0)^2 - \frac{2}{\sigma^2}(R - R_0)^2\right)$.

4. RESULTS AND DISCUSSION

4.1. Spin-Boson Model. The results for the spin-boson model are shown in Figure 2. The quantum-mechanically exact results for this case were calculated via the dissipation equation of motion (DEOM) method of Yan et al.[108] Inspection of the results gives rise to the following observations:

- The LSCI, LSCII, and Ehrenfest methods are the least accurate methods. Interestingly, while those methods are able to reproduce $\langle \hat{\sigma}_z(t) \rangle$ and $\langle \hat{\sigma}_y(t) \rangle$ rather accurately for the high-temperature, symmetric model, this is not the case for $\langle \hat{\sigma}_x(t) \rangle$.
- The mLSC/$\phi^1\phi^1$, mLSC/$\phi^1\phi^2$, and mLSC/$\phi^2\phi^2$ methods are the most accurate. Notably, for $\langle \hat{\sigma}_x(t) \rangle$ in the symmetric low T case, mLSC/$\phi^2\phi^2$ is seen to be significantly more accurate than mLSC/$\phi^1\phi^1$ and mLSC/$\phi^1\phi^2$.
- Both the mLSC methods and SQC constitute an improvement over LSCI and LSCII. mLSC/$\phi^1\phi^1$, mLSC/$\phi^1\phi^2$, and mLSC/$\phi^2\phi^2$ perform at least as well as SQC in all cases, often yielding more accurate results.

These observations demonstrate the importance of comparing the dynamics of the entire electronic density matrix, as opposed to just the populations (as captured by $\langle \hat{\sigma}_z(t) \rangle$). They also point to mLSC/$\phi^1\phi^1$, mLSC/$\phi^1\phi^2$, and mLSC/$\phi^2\phi^2$ as the methods of choice, since they are more accurate than LSCI and LSCII and do not involve choices regarding window shape and width in SQC.

In addition to considering the correlation functions shown in Figure 2, we can further analyze these results by breaking each into constituent correlation functions. The LSCI, LSCII, and modified LSC correlation functions in Figure 2 are each calculated as a sum of two constituents, such that

$$\langle \hat{\sigma}_i(t) \rangle = C_{|1\rangle\langle 1|\hat{\sigma}_i}(t) = \frac{1}{2}(C_{\hat{1}\hat{\sigma}_i}(t) + C_{\hat{\sigma}_z\hat{\sigma}_i}(t)) \tag{32}$$

where $i \in \{x, y, z\}$. Note that as per eq 7, $\hat{Q}_1 \equiv \hat{\sigma}_z$. Plots of the full Pauli-space of correlation functions computed can be found in the Supporting Information. Notably, in the case of the spin-boson systems studied here, LSCI and LSCII actually perform extremely well for correlation functions of the form $C_{\hat{\sigma}_i\hat{\sigma}_j}(t)$ but have larger errors for correlation functions of the form $C_{\hat{1}\hat{\sigma}_i}(t)$.

https://dx.doi.org/10.1021/acs.jctc.9b01267
J. Chem. Theory Comput. 2020, 16, 2883−2895

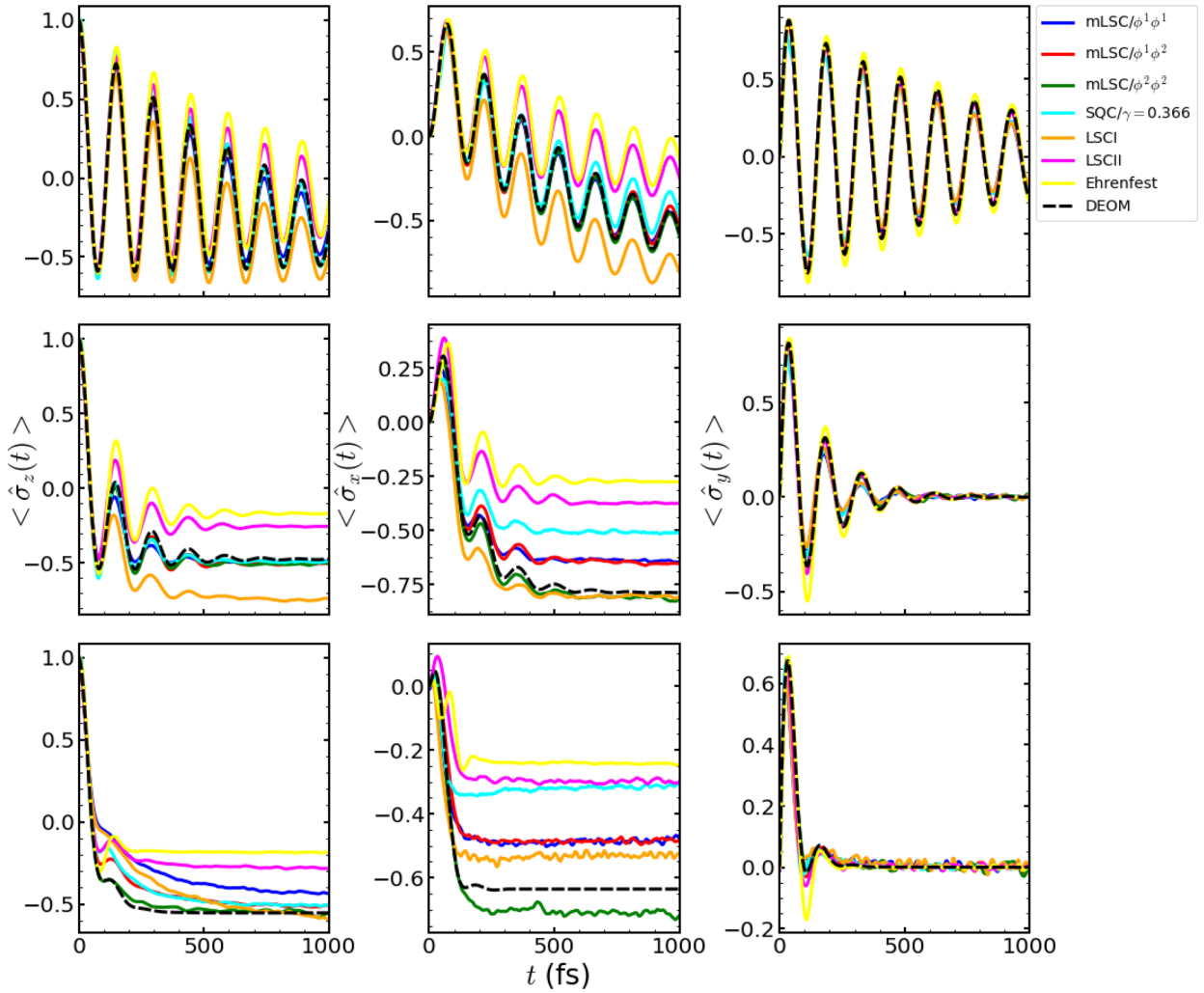

Figure 3. Population and coherence dynamics of 2-site exciton models at $\epsilon_1 = 50$ cm^{-1}, $\epsilon_2 = -50$ cm^{-1}, $\Delta = 100$ cm^{-1}, $\omega_c = 200$ cm^{-1}, $T = 72$ K, and $\zeta = 10$, 50, and 150 cm^{-1} (from top to bottom). Here for SQC, we employ triangular windows with width $\gamma = 0.366$. (We also checked square windows with the same width and have not found obvious differences between the two results.)

The fact that the inaccuracy of the traditional mapping approaches, LSCI and LSCII, is isolated to the identity containing correlation functions explains the drastic increase in accuracy achieved by the modified mapping approaches, given that the latter are based on a different treatment of this operator.

For the critical damping parameter set mentioned above, we note that these observations appear to also apply. We report the results in Figure S5 of the Supporting Information.

4.2. Frenkel Biexciton Model. The results for the Frenkel biexciton model are shown in Figure 3. Exact results for this model were adopted from ref 79, where they were calculated using the HEOM method. We also note that SQC results for this model were previously reported by Cotton and Miller.[60,80] However, the model parameters used in refs 60 and 80 were $\omega_c/\Delta = 0.53$ and 0.106, which correspond to the slow bath limit, and $k_BT/\Delta \sim 2$ ($T = 300$ K and $\Delta = 100$ cm^{-1}), which corresponds to the high-temperature limit. In contrast, here we consider model parameters that correspond to the fast bath limit, $\omega_c/\Delta = 2$, and the low temperature limit, $k_BT/\Delta \sim 0.5$, which are expected to provide a more challenging test case for the approximate methods under consideration. For those model parameters, we report results obtained for three values of electron−phonon coupling coefficients: $\zeta/\Delta = 0.1$, 0.5, and 1.5.

The results are plotted in Figure 3. Inspection of the results gives rise to the following observations:

- For $\langle\hat{\sigma}_z(t)\rangle$, mLSC/$\phi^1\phi^1$, mLSC/$\phi^1\phi^2$, mLSC/$\phi^2\phi^2$, and SQC are accurate at the weak electron−phonon coupling regime ($\zeta = 10$ cm^{-1}) but become increasingly inaccurate with increasing electron−phonon coupling strength ($\zeta = 150$ cm^{-1}). This is because one would need a quantum description of the bath modes in this limit. Somewhat surprisingly, the prediction for $\langle\hat{\sigma}_z(t)\rangle$ obtained via the mLSC/$\phi^2\phi^2$ method is seen to nearly coincide with the exact results for all coupling strengths. Finally, the accuracy of $\langle\hat{\sigma}_z(t)\rangle$ predicted by the LSCI, LSCII, and Ehrenfest methods is seen to deteriorate with increasing time.
- For $\langle\hat{\sigma}_x(t)\rangle$, all methods are seen to capture the initial dynamics rather well but deteriorate in accuracy with increasing time. This can be attributed to the quantum nature of the nuclear DOFs in the fast bath and low temperature limits. However, for weak electron−phonon coupling, mLSC/$\phi^1\phi^1$, mLSC/$\phi^1\phi^2$, mLSC/$\phi^2\phi^2$, and SQC are seen to be rather accurate throughout the entire simulation time, while LSCI, LSCII, and Ehrenfest are

https://dx.doi.org/10.1021/acs.jctc.9b01267
J. Chem. Theory Comput. 2020, 16, 2883−2895

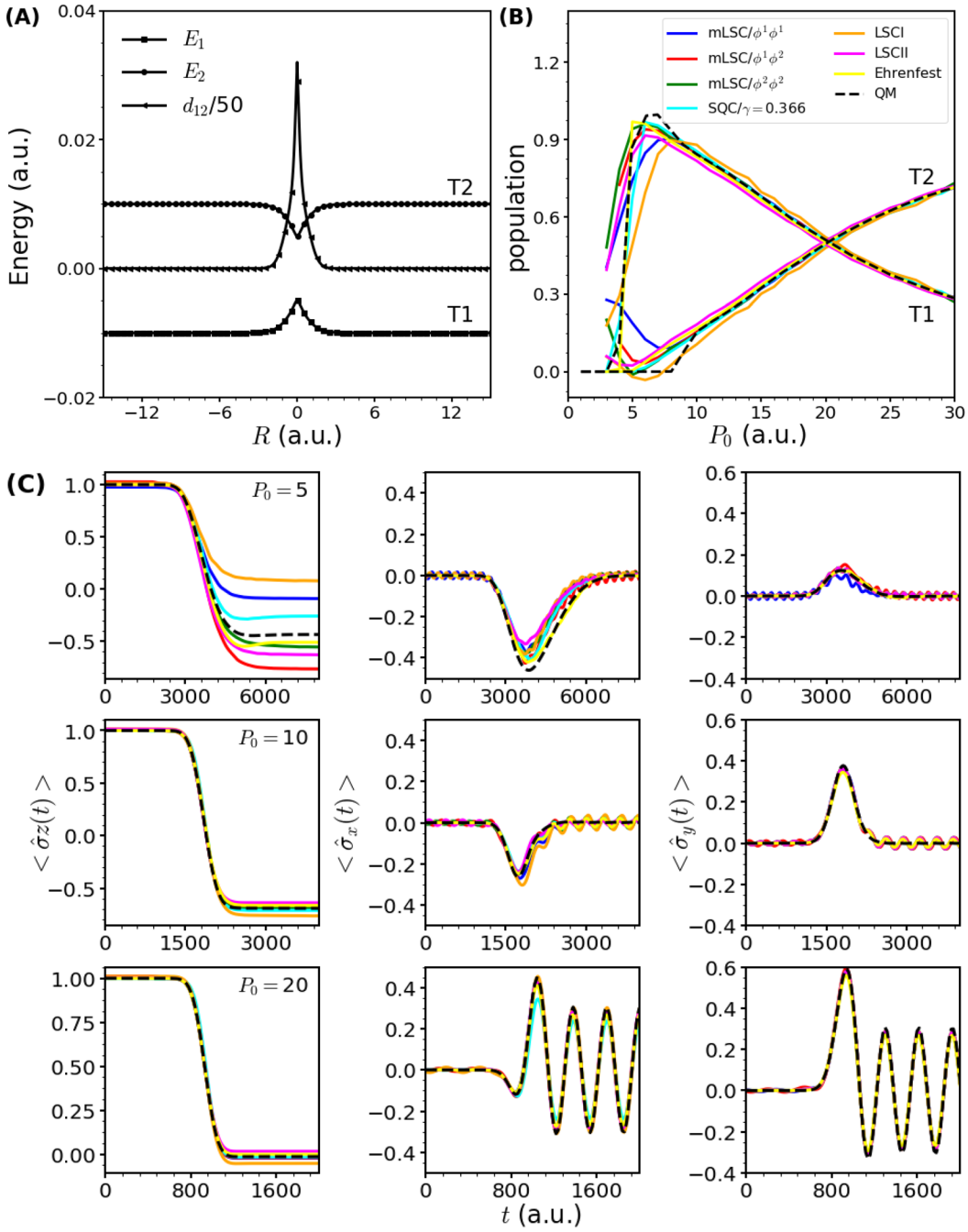

Figure 4. Tully's model of single avoided crossing. Panel A: adiabatic potential energy curves (E_1 and E_2) and first-order nonadiabatic coupling strength (d_{12}). Panel B: population versus initial momentum of the wavepacket which started from the left side of the ground state. The wavepacket transmission at the lower and upper energy curves are denoted as T1 and T2, respectively. Panel C: population and coherence dynamics with P_0 = 5, 10, and 20. In SQC, we employ triangular windows with width γ = 0.366. The total number of trajectories is 10^5.

seen to significantly deviate from the exact results on the same time scale. Finally, mLSC/$\phi^2\phi^2$ is again seen to provide the most accurate results when the electron–phonon coupling strength is increased.

- For $\langle\hat{\sigma}_y(t)\rangle$, all of the methods under consideration are seen to give a more reasonable description of the exact results.

As for the spin-boson model, those observations demonstrate the importance of comparing the dynamics of the entire electronic density matrix, as opposed to just the populations (as captured by $\langle\hat{\sigma}_z(t)\rangle$). They also point to mLSC/$\phi^2\phi^2$ as the method of choice.

4.3. Tully's Models 1 and 2. The results for the single avoided crossing and dual avoided crossing Tully's models 1 and 2 are shown in Figures 4 and 5, respectively. Panels (A) in these figures show the adiabatic ground and excited energies (E_1 and E_2, respectively) and the nonadiabatic coupling coefficient (d_{12}). Panels (B) of these figures show that all the methods under consideration reproduce the quantum-mechanically exact asymptotic populations rather accurately when P_0 > 10, i.e., when the description of the nuclear DOFs as classical becomes

https://dx.doi.org/10.1021/acs.jctc.9b01267
J. Chem. Theory Comput. 2020, 16, 2883−2895

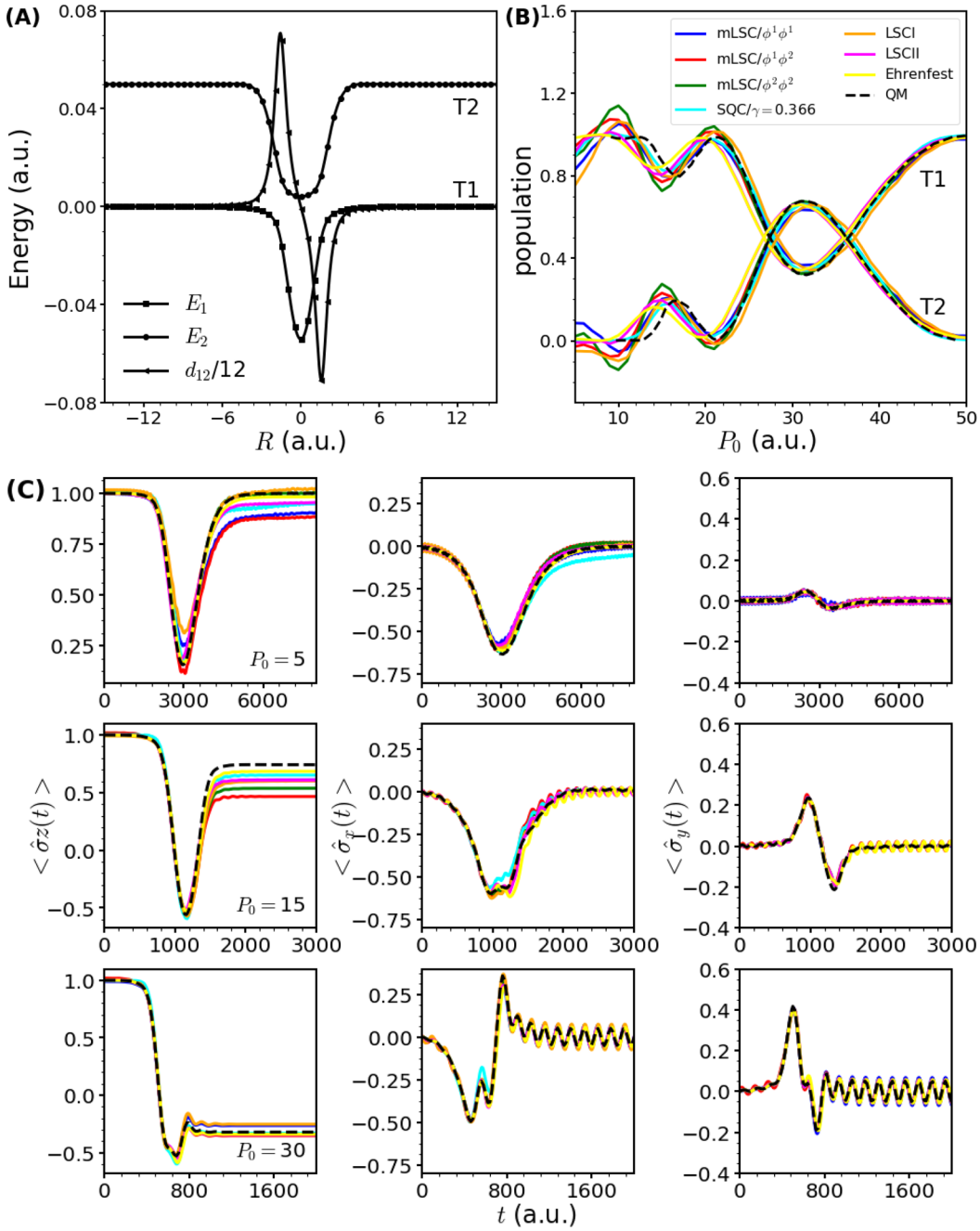

Figure 5. Tully's model of dual avoided crossing. As described in Figure 4 except for panel C, P_0 = 5, 15, and 30.

justified. The results for $\langle \hat{\sigma}_z(t) \rangle$ in Panels (C) of these figures show that the methods accurately reproduce not just the final populations but also their intermediate dynamics, when $P_0 > 10$. Furthermore, the results for $\langle \hat{\sigma}_x(t) \rangle$ and $\langle \hat{\sigma}_y(t) \rangle$ reveal that the methods also reproduce the quantum-mechanically exact coherences rather accurately. Results for Tully's model 3 (extended coupling) are not reported since none of the methods discussed in this paper are able to produce a reasonable description of the quantum dynamics for this challenging model.

It should be noted that the mLSC methods do not yield a major improvement in this case, although they also do not significantly degrade the quality of the results.

5. CONCLUDING REMARKS

Various QC/MH methods for simulating electronically nonadiabatic molecular dynamics have been proposed over the last two decades, which are based on MMST mapping variables, but differ with respect to the way in which the operators are evaluated at different times. The comprehensive comparison presented in this paper aims at estimating the relative accuracy of several of those methods. This is made possible by the availability of quantum-mechanically exact results for the benchmark models under consideration and extending the comparison beyond the electronic populations to electronic coherences.

The above-mentioned comparison lends further weight to the modified LSC methods recently introduced by Saller, Kelly, and Richardson[62,63] (mLSC/$\phi^1\phi^1$, mLSC/$\phi^1\phi^2$, and mLSC/$\phi^2\phi^2$),

https://dx.doi.org/10.1021/acs.jctc.9b01267
J. Chem. Theory Comput. 2020, 16, 2883−2895

which are shown to be significantly more accurate in comparison to the more traditional LSCI, LSCII, and Ehrenfest methods. The accuracy of the mLSC methods is also comparable to that of SQC, even exceeding it in certain cases. Among the modified LSC methods, mLSC/$\phi^2\phi^2$ appears to be somewhat more accurate in comparison to mLSC/$\phi^1\phi^1$ and mLSC/$\phi^1\phi^2$, although results for different benchmarks[63] suggest this is not always the case.

Comparing the performance of the mLSC approaches to SQC, it could be argued that since the SQC windows prevent averaging of trajectories which have strayed into unphysical regions of phase space, therefore preventing spurious nuclear dynamics, SQC might be expected to perform better in scattering type problems such as the Tully's models studied here and can be applied with photoexcited problems with extra adjustments.[109] The mLSC methods, on the other hand, appear to perform better than SQC for condensed phase problems.

It should be noted that the enhanced accuracy of the mLSC methods does not come at the expense of computational cost, which remains comparable to that of the Ehrenfest, LSCI, and LSCII methods. It would therefore be highly desirable to extend the range of applicability and accessibility of the mLSC methods to complex molecular system, as well as to the calculation of quantities other than the electronic populations and coherences. Work toward those goals is currently underway in our groups and will be reported in future papers.

■ ASSOCIATED CONTENT

Supporting Information

The Supporting Information is available free of charge at https://pubs.acs.org/doi/10.1021/acs.jctc.9b01267.

Prescriptions for construction of correlation functions for mapping methods studied here, extended set of results for spin-boson systems studied above as well as results for additional parameter set, which corresponds to critical damping regime (PDF)

■ AUTHOR INFORMATION

Corresponding Author

Eitan Geva − *Department of Chemistry, University of Michigan, Ann Arbor, Michigan 48109, United States;* orcid.org/0000-0002-7935-4586; Email: eitan@umich.edu

Authors

Xing Gao − *Department of Chemistry, University of Michigan, Ann Arbor, Michigan 48109, United States*

Maximilian A. C. Saller − *Laboratory of Physical Chemistry, ETH Zürich, 8093 Zürich, Switzerland*

Yudan Liu − *Department of Chemistry, University of Michigan, Ann Arbor, Michigan 48109, United States*

Aaron Kelly − *Department of Chemistry, Dalhousie University, Halifax, Nova Scotia, Canada*

Jeremy O. Richardson − *Laboratory of Physical Chemistry, ETH Zürich, 8093 Zürich, Switzerland*

Complete contact information is available at: https://pubs.acs.org/10.1021/acs.jctc.9b01267

Notes

The authors declare no competing financial interest.

■ ACKNOWLEDGMENTS

E.G. is grateful for support from NSF via Grants CHE-1800325 and CHE-1663636 and computational resources and services provided by Advanced Research Computing at the University of Michigan, Ann Arbor. A.K. acknowledges support from an NSERC Discovery Grant. J.O.R. and M.A.C.S. acknowledge support from the Swiss National Science Foundation through the NCCR MUST (Molecular Ultrafast Science and Technology) Network. M.A.C.S. would like to acknowledge support through the ETH postdoctoral fellowship.

■ REFERENCES

(1) Xu, D.; Schulten, K. Coupling of protein motion to electron transfer in a photosynthetic reaction center: investigating the low temperature behavior in the framework of the spin−boson model. *Chem. Phys.* **1994**, *182*, 91−117.

(2) Ishizaki, A.; Fleming, G. R. Quantum Coherence in Photosynthetic Light Harvesting. *Annu. Rev. Condens. Matter Phys.* **2012**, *3*, 333−361.

(3) Liddell, P. A.; Kuciauskas, D.; Sumida, J. P.; Nash, B.; Nguyen, D.; Moore, A. L.; Moore, T. A.; Gust, D. Photoinduced charge separation and charge recombination to a triplet state in a carotene-porphyrin-fullerene triad. *J. Am. Chem. Soc.* **1997**, *119*, 1400−1405.

(4) Liddell, P. A.; Kodis, G.; Moore, A. L.; Moore, T. A.; Gust, D. Photo switching of photoinduced electron transfer in a dithienylethene-porphyrin-fullerene triad molecule. *J. Am. Chem. Soc.* **2002**, *124*, 7668−7669.

(5) Brédas, J.-L.; Beljonne, D.; Coropceanu, V.; Cornil, J. Charge-Transfer and Energy-Transfer Processes in π-Conjugated Oligomers and Polymers: A Molecular Picture. *Chem. Rev.* **2004**, *104*, 4971−5004.

(6) Rizzi, A. C.; van Gastel, M.; Liddell, P. A.; Palacios, R. E.; Moore, G. F.; Kodis, G.; Moore, A. L.; Moore, T. A.; Gust, D.; Braslavsky, S. E. Entropic changes control the charge separation process in triads mimicking photosynthetic charge separation. *J. Phys. Chem. A* **2008**, *112*, 4215−4223.

(7) Tian, H.; Yu, Z.; Hagfeldt, A.; Kloo, L.; Sun, L. Organic Redox Couples and Organic Counter Electrode for Efficient Organic Dye-Sensitized Solar Cells. *J. Am. Chem. Soc.* **2011**, *133*, 9413−9422.

(8) Mishra, A.; Fischer, M. K. R.; Bäuerle, P. Metal-Free Organic Dyes for Dye-Sensitized Solar Cells: From Structure: Property Relationships to Design Rules. *Angew. Chem., Int. Ed.* **2009**, *48*, 2474−2499.

(9) Feldt, S. M.; Gibson, E. A.; Gabrielsson, E.; Sun, L.; Boschloo, G.; Hagfeldt, A. Design of Organic Dyes and Cobalt Polypyridine Redox Mediators for High-Efficiency Dye-Sensitized Solar Cells. *J. Am. Chem. Soc.* **2010**, *132*, 16714−16724.

(10) Zhao, Y.; Liang, W. Charge transfer in organic molecules for solar cells: Theoretical perspective. *Chem. Soc. Rev.* **2012**, *41*, 1075−1087.

(11) Lee, M. H.; Dunietz, B. D.; Geva, E. Calculation From First Principles of Intramolecular Golden-Rule Rate Constants for Photo-Induced Electron Transfer in Molecular Donor-Acceptor Systems. *J. Phys. Chem. C* **2013**, *117*, 23391−23401.

(12) Lee, M. H.; Dunietz, B. D.; Geva, E. Donor-to-Donor vs. Donor-to-Acceptor Interfacial Charge Transfer States in the Phthalocyanine-Fullerene Organic Photovoltaic System. *J. Phys. Chem. Lett.* **2014**, *5*, 3810−3816.

(13) Wang, Y.; Suzuki, H.; Xie, J.; Tomita, O.; Martin, D. J.; Higashi, M.; Kong, D.; Abe, R.; Tang, J. Mimicking Natural Photosynthesis: Solar to Renewable H 2Fuel Synthesis by Z-Scheme Water Splitting Systems. *Chem. Rev.* **2018**, *118*, 5201−5241.

(14) Sun, X.; Zhang, P.; Lai, Y.; Williams, K. L.; Cheung, M. S.; Dunietz, B. D.; Geva, E. Computational Study of Charge-Transfer Dynamics in the Carotenoid−Porphyrin−C_{60} Molecular Triad Solvated in Explicit Tetrahydrofuran and Its Spectroscopic Signature. *J. Phys. Chem. C* **2018**, *122*, 11288−11299.

(15) Lee, M. H.; Dunietz, B. D.; Geva, E. Calculation from First Principles of Golden-Rule Rate Constants for Photo-Induced Subphthalocyanine/Fullerene Interfacial Charge Transfer and Recom-

bination in Organic Photovoltaic Cells. *J. Phys. Chem. C* **2014**, *118*, 9780−9789.
(16) Novoderezhkin, V. I.; Yakovlev, A. G.; van Grondelle, R.; Shuvalov, V. A. Coherent Nuclear and Electronic Dynamics in Primary Charge Separation in Photosynthetic Reaction Centers: A Redfield Theory Approach. *J. Phys. Chem. B* **2004**, *108*, 7445−7457.
(17) Jang, S. J.; Mennucci, B. Delocalized excitons in natural light-harvesting complexes. *Rev. Mod. Phys.* **2018**, *90*, 1129−49.
(18) Segatta, F.; Cupellini, L.; Garavelli, M.; Mennucci, B. Quantum Chemical Modeling of the Photoinduced Activity of Multichromophoric Biosystems. *Chem. Rev.* **2019**, *119*, 9361−9380.
(19) Meyer, H.-D.; Miller, W. H. A classical analog for electronic degrees of freedom in nonadiabatic collision processes. *J. Chem. Phys.* **1979**, *70*, 3214−3223.
(20) Kosloff, R. Propagation methods for quantum molecular dynamics. *Annu. Rev. Phys. Chem.* **1994**, *45*, 145.
(21) Meyer, H.-D.; Gatti, F.; Worth, G. A. *Multidimensional Quantum Dynamics; MCTDH Theory and Applications*; John Wiley & Sons: 2009; DOI: 10.1002/9783527627400.
(22) Greene, S. M.; Batista, V. S. Tensor-Train Split-Operator Fourier Transform (TT-SOFT) Method: Multidimensional Nonadiabatic Quantum Dynamics. *J. Chem. Theory Comput.* **2017**, *13*, 4034−4042.
(23) Stock, G.; Thoss, M. Classical description of nonadiabatic quantum dynamics. *Adv. Chem. Phys.* **2005**, *131*, 243−376.
(24) McLachlan, A. A variational solution of the time-dependent Schrodinger equation. *Mol. Phys.* **1964**, *8*, 39−44.
(25) Tully, J. C. Molecular dynamics with electronic transitions. *J. Chem. Phys.* **1990**, *93*, 1061−1071.
(26) Tully, J. C.; Preston, R. K. Trajectory surface hopping approach to nonadiabatic molecular collisions: Reaction of H^+ with D_2. *J. Chem. Phys.* **1971**, *55*, 562−572.
(27) Bittner, E. R.; Rossky, P. J. Quantum decoherence in mixed quantum classical systems: Nonadiabatic processes. *J. Chem. Phys.* **1995**, *103*, 8130−8143.
(28) Prezhdo, O. V.; Rossky, P. J. Evaluation of quantum transition rates from quantum-classical molecular dynamics simulations. *J. Chem. Phys.* **1997**, *107*, 5863−5878.
(29) Horenko, I.; Salzmann, C.; Schmidt, B.; Schutte, C. Quantum-classical Liouville approach to molecular dynamics: Surface hopping Gaussian phase-space packets. *J. Chem. Phys.* **2002**, *117*, 11075−11088.
(30) Subotnik, J. E.; Shenvi, N. A new approach to decoherence and momentum rescaling in the surface hopping algorithm. *J. Chem. Phys.* **2011**, *134*, 024105−19.
(31) Shushkov, P.; Li, R.; Tully, J. C. Ring polymer molecular dynamics with surface hopping. *J. Chem. Phys.* **2012**, *137*, 22A549.
(32) Wang, L.; Trivedi, D.; Prezhdo, O. V. Global Flux Surface Hopping Approach for Mixed Quantum-Classical Dynamics. *J. Chem. Theory Comput.* **2014**, *10*, 3598−3605.
(33) Jaeger, H. M.; Fischer, S.; Prezhdo, O. V. Decoherence-induced surface hopping. *J. Chem. Phys.* **2012**, *137*, 22A545.
(34) Wang, L.; Prezhdo, O. V. A Simple Solution to the Trivial Crossing Problem in Surface Hopping. *J. Phys. Chem. Lett.* **2014**, *5*, 713−719.
(35) Ouyang, W.; Dou, W.; Subotnik, J. E. Surface hopping with a manifold of electronic states. I. Incorporating surface-leaking to capture lifetimes. *J. Chem. Phys.* **2015**, *142*, 084109−13.
(36) Bedard-Hearn, M. J.; Larsen, R. E.; Schwartz, B. J. Mean-field dynamics with stochastic decoherence (MF-SD): A new algorithm for nonadiabatic mixed quantum/classical molecular-dynamics simulations with nuclear-induced decoherence. *J. Chem. Phys.* **2005**, *123*, 234106−17.
(37) Martens, C. C.; Fang, J. Semiclassical-limit molecular dynamics on multiple electronic surfaces. *J. Chem. Phys.* **1997**, *106*, 4918−4930.
(38) Donoso, A.; Martens, C. C. Simulation of coherent nonadiabatic dynamics using classical trajectories. *J. Phys. Chem. A* **1998**, *102*, 4291.
(39) Kapral, R.; Ciccotti, G. Mixed quantum-classical dynamics. *J. Chem. Phys.* **1999**, *110*, 8919−8929.
(40) Nielsen, S.; Kapral, R.; Ciccotti, G. Mixed quantum-classical surface hopping dynamics. *J. Chem. Phys.* **2000**, *112*, 6543−6553.
(41) Shi, Q.; Geva, E. A derivation of the mixed quantum-classical Liouville equation from the influence functional formalism. *J. Chem. Phys.* **2004**, *121*, 3393−3404.
(42) MacKernan, D.; Kapral, R.; Ciccotti, G. Sequential short-time propagation of quantum-classical dynamics. *J. Phys.: Condens. Matter* **2002**, *14*, 9069−9076.
(43) Mac Kernan, D.; Ciccotti, G.; Kapral, R. Trotter-Based Simulation of Quantum-Classical Dynamics. *J. Phys. Chem. B* **2008**, *112*, 424−432.
(44) Nassimi, A.; Bonella, S.; Kapral, R. Analysis of the quantum-classical Liouville equation in the mapping basis. *J. Chem. Phys.* **2010**, *133*, 134115−11.
(45) Lambert, R.; Makri, N. Quantum-classical path integral. I. Classical memory and weak quantum nonlocality. *J. Chem. Phys.* **2012**, *137*, 22A552.
(46) Lambert, R.; Makri, N. Quantum-classical path integral. II. Numerical methodology. *J. Chem. Phys.* **2012**, *137*, 22A553−12.
(47) Banerjee, T.; Makri, N. Quantum-Classical Path Integral with Self-Consistent Solvent-Driven Reference Propagators. *J. Phys. Chem. B* **2013**, *117*, 13357−13366.
(48) Makri, N. Quantum-classical path integral: A rigorous approach to condensed phase dynamics. *Int. J. Quantum Chem.* **2015**, *115*, 1209−1214.
(49) Walters, P. L.; Makri, N. Quantum−Classical Path Integral Simulation of Ferrocene−Ferrocenium Charge Transfer in Liquid Hexane. *J. Phys. Chem. Lett.* **2015**, *6*, 4959−4965.
(50) Walters, P. L.; Makri, N. Iterative quantum-classical path integral with dynamically consistent state hopping. *J. Chem. Phys.* **2016**, *144*, 044108−9.
(51) Stock, G.; Thoss, M. Semiclassical Description of Nonadiabatic Quantum Dynamics. *Phys. Rev. Lett.* **1997**, *78*, 578−581.
(52) Sun, X.; Wang, H.; Miller, W. H. Semiclassical theory of electronically nonadiabatic dynamics: Results of a linearized approximation to the initial value representation. *J. Chem. Phys.* **1998**, *109*, 7064.
(53) Wang, H.; Song, X.; Chandler, D.; Miller, W. H. Semiclassical study of electronically nonadiabatic dynamics in the condensed-phase: Spin-boson problem with Debye spectral density. *J. Chem. Phys.* **1999**, *110*, 4828−4840.
(54) Swenson, D. W. H.; Levy, T.; Cohen, G.; Rabani, E.; Miller, W. H. Application of a semiclassical model for the second-quantized many-electron Hamiltonian to nonequilibrium quantum transport: The resonant level model. *J. Chem. Phys.* **2011**, *134*, 164103−9.
(55) Kelly, A.; van Zon, R.; Schofield, J.; Kapral, R. Mapping quantum-classical Liouville equation: Projectors and trajectories. *J. Chem. Phys.* **2012**, *136*, 084101−13.
(56) Cotton, S. J.; Miller, W. H. Symmetrical windowing for quantum states in quasi-classical trajectory simulations: Application to electronically non-adiabatic processes. *J. Chem. Phys.* **2013**, *139*, 234112−10.
(57) Cotton, S. J.; Miller, W. H. Symmetrical Windowing for Quantum States in Quasi-Classical Trajectory Simulations. *J. Phys. Chem. A* **2013**, *117*, 7190−7194.
(58) Cotton, S. J.; Igumenshchev, K.; Miller, W. H. Symmetrical windowing for quantum states in quasi-classical trajectory simulations: Application to electron transfer. *J. Chem. Phys.* **2014**, *141*, 084104−11.
(59) Cotton, S. J.; Miller, W. H. A Symmetrical Quasi-Classical Spin-Mapping Model for the Electronic Degrees of Freedom in Non-Adiabatic Processes. *J. Phys. Chem. A* **2015**, *119*, 12138−12145.
(60) Cotton, S. J.; Miller, W. H. The Symmetrical Quasi-Classical Model for Electronically Non-Adiabatic Processes Applied to Energy Transfer Dynamics in Site-Exciton Models of Light-Harvesting Complexes. *J. Chem. Theory Comput.* **2016**, *12*, 983−991.
(61) Cotton, S. J.; Miller, W. H. A new symmetrical quasi-classical model for electronically non-adiabatic processes: Application to the case of weak non-adiabatic coupling. *J. Chem. Phys.* **2016**, *145*, 144108−17.
(62) Saller, M. A. C.; Kelly, A.; Richardson, J. O. On the identity of the identity operator in nonadiabatic linearized semiclassical dynamics. *J. Chem. Phys.* **2019**, *150*, 071101−8.

(63) Saller, M. A.; Kelly, A.; Richardson, J. O. Improved population operators for multi-state nonadiabatic dynamics with the mixed quantum-classical mapping approach. *Faraday Discuss.* **2020**, *221*, 150−167.
(64) Tao, G. Electronically Nonadiabatic Dynamics in Singlet Fission: A Quasi-Classical Trajectory Simulation. *J. Phys. Chem. C* **2014**, *118*, 17299−17305.
(65) Tao, G. A multi-state trajectory method for non-adiabatic dynamics simulations. *J. Chem. Phys.* **2016**, *144*, 094108−9.
(66) Tao, G.; Shen, N. Mapping State Space to Quasiclassical Trajectory Dynamics in Coherence-Controlled Nonadiabatic Simulations for Condensed Phase Problems. *J. Phys. Chem. A* **2017**, *121*, 1734−1747.
(67) Tao, G. Nonadiabatic Dynamics of Hydrogen Diffusion on Cu(001): Classical Mapping Model with Multistate Projection Window in Real Space. *ChemPhysChem* **2019**, *62*, 2127−2135.
(68) Liu, J. A unified theoretical framework for mapping models for the multi-state Hamiltonian. *J. Chem. Phys.* **2016**, *145*, 204105−15.
(69) He, X.; Liu, J. A new perspective for nonadiabatic dynamics with phase space mapping models. *J. Chem. Phys.* **2019**, *151*, 024105−22.
(70) Runeson, J. E.; Richardson, J. O. Spin-mapping approach for nonadiabatic molecular dynamics. *J. Chem. Phys.* **2019**, *151*, 044119.
(71) Huo, P.; Coker, D. F. Communication: Partial linearized density matrix dynamics for dissipative, non-adiabatic quantum evolution. *J. Chem. Phys.* **2011**, *135*, 201101.
(72) Hsieh, C.-Y.; Kapral, R. Nonadiabatic dynamics in open quantum-classical systems: Forward-backward trajectory solution. *J. Chem. Phys.* **2012**, *137*, 22A507−11.
(73) Hsieh, C.-Y.; Kapral, R. Analysis of the forward-backward trajectory solution for the mixed quantum-classical Liouville equation. *J. Chem. Phys.* **2013**, *138*, 134110−12.
(74) Thoss, M.; Wang, H.; Miller, W. H. Generalized forward-backward initial value representation for the calculation of correlation functions in complex systems. *J. Chem. Phys.* **2001**, *114*, 9220−9235.
(75) Burant, J. C.; Batista, V. S. Real time path integrals using the Herman−Kluk propagator. *J. Chem. Phys.* **2002**, *116*, 2748−2756.
(76) Bonfanti, M.; Tantardini, G. F.; Hughes, K. H.; Martinazzo, R.; Burghardt, I. Compact MCTDH Wave Functions for High-Dimensional System-Bath Quantum Dynamics. *J. Phys. Chem. A* **2012**, *116*, 11406−11413.
(77) Wu, Y.; Batista, V. S. Matching-pursuit for simulations of quantum processes. *J. Chem. Phys.* **2003**, *118*, 6720−6724.
(78) Greene, S. M.; Batista, V. S. Tensor-train split-operator fourier transform (TT-SOFT) method: Multidimensional nonadiabatic quantum dynamics. *J. Chem. Theory Comput.* **2017**, *13*, 4034−4042.
(79) Ishizaki, A.; Fleming, G. R. On the adequacy of the Redfield equation and related approaches to the study of quantum dynamics in electronic energy transfer. *J. Chem. Phys.* **2009**, *130*, 234110−9.
(80) Miller, W. H.; Cotton, S. J. Communication: Wigner functions in action-angle variables, Bohr-Sommerfeld quantization, the Heisenberg correspondence principle, and a symmetrical quasi-classical approach to the full electronic density matrix. *J. Chem. Phys.* **2016**, *145*, 081102−5.
(81) Kim, H.; Nassimi, A.; Kapral, R. Quantum-classical Liouville dynamics in the mapping basis. *J. Chem. Phys.* **2008**, *129*, 084102.
(82) Cotton, S. J.; Liang, R.; Miller, W. H. On the adiabatic representation of Meyer-Miller electronic-nuclear dynamics. *J. Chem. Phys.* **2017**, *147*, 064112−11.
(83) Thoss, M.; Stock, G. Mapping approach to the semiclassical description of nonadiabatic quantum dynamics. *Phys. Rev. A: At., Mol., Opt. Phys.* **1999**, *59*, 64−79.
(84) Stock, G.; Müller, U. Flow of zero-point energy and exploration of phase space in classical simulations of quantum relaxation dynamics. *J. Chem. Phys.* **1999**, *111*, 65−76.
(85) Miller, W. H. The semiclassical initial value representation: A potentially practical way for adding quantum effects to classical molecular dynamics simulations. *J. Phys. Chem. A* **2001**, *105*, 2942−2955.
(86) Ananth, N.; Venkataraman, C.; Miller, W. H. Semiclassical description of electronically nonadiabatic dynamics via the initial value representation. *J. Chem. Phys.* **2007**, *127*, 084114−10.
(87) Miller, W. H.; Cotton, S. J. Classical molecular dynamics simulation of electronically non-adiabatic processes. *Faraday Discuss.* **2016**, *195*, 9−30.
(88) Ananth, N.; Miller, T. F., III Exact quantum statistics for electronically nonadiabatic systems using continuous path variables. *J. Chem. Phys.* **2010**, *133*, 234103.
(89) Ananth, N. Mapping variable ring polymer molecular dynamics: A path-integral based method for nonadiabatic processes. *J. Chem. Phys.* **2013**, *139*, 124102.
(90) Richardson, J. O.; Thoss, M. Communication: Nonadiabatic ring-polymer molecular dynamics. *J. Chem. Phys.* **2013**, *139*, 031102.
(91) Richardson, J. O.; Meyer, P.; Pleinert, M.-O.; Thoss, M. An analysis of nonadiabatic ring-polymer molecular dynamics and its application to vibronic spectra. *Chem. Phys.* **2017**, *482*, 124−134.
(92) Meyer, H.-D.; Miller, W. H. Classical models for electronic degrees of freedom: Derivation via spin analogy and application to $F^* + H_2 \rightarrow F + H_2$. *J. Chem. Phys.* **1979**, *71*, 2156−2169.
(93) Cotton, S. J.; Miller, W. H. A symmetrical quasi-classical spin-mapping model for the electronic degrees of freedom in non-adiabatic processes. *J. Phys. Chem. A* **2015**, *119*, 12138−12145.
(94) Thoss, M.; Stock, G. Mapping approach to the semiclassical description of nonadiabatic quantum dynamics. *Phys. Rev. A: At., Mol., Opt. Phys.* **1999**, *59*, 64−79.
(95) Shi, Q.; Geva, E. A semiclassical theory of vibrational energy relaxation in the condensed phase. *J. Phys. Chem. A* **2003**, *107*, 9059−9069.
(96) Shi, Q.; Geva, E. Vibrational energy relaxation in liquid oxygen from a semiclassical molecular dynamics simulation. *J. Phys. Chem. A* **2003**, *107*, 9070−9078.
(97) Shi, Q.; Geva, E. A semiclassical generalized quantum master equation for an arbitrary system-bath coupling. *J. Chem. Phys.* **2004**, *120*, 10647−10658.
(98) Shi, Q.; Geva, E. Nonradiative electronic relaxation rate constants from approximations based on linearizing the path-integral forward-backward action. *J. Phys. Chem. A* **2004**, *108*, 6109−6116.
(99) Shi, Q.; Geva, E. A comparison between different semiclassical approximations for optical response functions in nonpolar liquid solutions. *J. Chem. Phys.* **2005**, *122*, 064506−10.
(100) Ka, B. J.; Shi, Q.; Geva, E. Vibrational energy relaxation rates via the linearized semiclassical approximations: Applications to neat diatomic liquids and atomic-diatomic liquid mixtures. *J. Phys. Chem. A* **2005**, *109*, 5527−5536.
(101) Ka, B. J.; Geva, E. Vibrational energy relaxation of polyatomic molecules in liquid solution via the linearized semiclassical method. *J. Phys. Chem. A* **2006**, *110*, 9555−9567.
(102) Shi, Q.; Geva, E. A comparison between different semiclassical approximations for optical response functions in nonpolar liquid solution II. The signature of excited state dynamics on two-dimensional spectra. *J. Chem. Phys.* **2008**, *129*, 124505.
(103) Vazquez, F. X.; Navrotskaya, I.; Geva, E. Vibrational energy relaxation rate constants via the linearized semiclassical method without force derivatives. *J. Phys. Chem. A* **2010**, *114*, 5682−5688.
(104) Vazquez, F. X.; Talapatra, S.; Geva, E. Vibrational Energy Relaxation in Liquid HCl and DCl via the Linearized Semiclassical Method: Electrostriction versus Quantum Delocalization. *J. Phys. Chem. A* **2011**, *115*, 9775−9781.
(105) McRobbie, P. L.; Geva, E. A benchmark study of different methods for calculating one- and two-dimensional optical spectra. *J. Phys. Chem. A* **2009**, *113*, 10425−10434.
(106) Wang, H.; Thoss, M. Theoretical study of ultrafast photo-induced electron transfer processes in mixed-valence systems. *J. Phys. Chem. A* **2003**, *107*, 2126−2136.
(107) Kelly, A.; Brackbill, N.; Markland, T. E. Accurate nonadiabatic quantum dynamics on the cheap: Making the most of mean field theory with master equations. *J. Chem. Phys.* **2015**, *142*, 094110−9.

https://dx.doi.org/10.1021/acs.jctc.9b01267
J. Chem. Theory Comput. 2020, 16, 2883−2895

(108) Yan, Y.; Jin, J.; Xu, R.-X.; Zheng, X. Dissipation equation of motion approach to open quantum systems. *Front. Phys.-Beijing* **2016**, *11*, 110306.
(109) Cotton, S. J.; Miller, W. H. Trajectory-adjusted electronic zero point energy in classical Meyer-Miller vibronic dynamics: Symmetrical quasiclassical application to photodissociation. *J. Chem. Phys.* **2019**, *150*, 194110.

https://dx.doi.org/10.1021/acs.jctc.9b01267
J. Chem. Theory Comput. 2020, 16, 2883−2895